

Improving aging and creep resistance in a dilute Al–Sc alloy by microalloying with Si, Zr and Er

N.Q. Vo^{a,c,*}, D.C. Dunand^{a,c}, D.N. Seidman^{a,b,c}

^a Department of Materials Science and Engineering, Northwestern University, Evanston, IL 60208, USA

^b Northwestern University Center for Atom-Probe Tomography, Northwestern University, Evanston, IL 60208, USA

^c NanoAl LLC, Skokie, IL 60077, USA

Received 5 April 2013; received in revised form 4 October 2013; accepted 7 October 2013

Available online 14 November 2013

Abstract

Nanosized precipitates in an Al–0.06Sc at.% alloy containing various microalloying additions were studied, with the goal of developing cost-effective aluminum alloys for high-temperature applications, using micro-hardness, electrical conductivity and atom-probe tomography measurements. Substituting 0.005 at.% Er for the more expensive Sc maintains high ambient-temperature strength, and dramatically improves the high-temperature creep resistance, as anticipated from the increase in lattice parameter mismatch between the α -Al(fcc) matrix and the coherent L1₂-ordered Al₃(Sc,Zr,Er) precipitates. A concentration of the slow-diffuser Zr as low as 0.02 at.% is sufficient to provide coarsening resistance at 400 °C (an homologous temperature of 0.72) for up to 66 days by forming a Zr-enriched outer shell encapsulating the precipitates. Finally, adding 0.05 at.% Si enhances ambient-temperature strength by increasing the number density of precipitates, while decreasing the homogenization and peak-aging heat-treatment times, which is caused by the Si atoms accelerating the Er and Sc diffusion kinetics. Si-containing alloys are also cost effective, owing to the existence of Si in commercial purity Al. But addition of Si reduces the precipitate coarsening resistance: the magnitude of this effect is, however, determined by the Si concentration.

© 2013 Acta Materialia Inc. Published by Elsevier Ltd. All rights reserved.

Keywords: Al–Sc–Er–Zr alloy; Atom-probe tomography; Strengthening; Optimization; High-temperature alloy

1. Introduction

The strong demand for low-density components in transport systems necessitates the design and fabrication of lightweight Al alloys for high-temperature applications (e.g., in and near engines and brakes), which do not lose their strength as a result of aging for long exposure times at elevated temperatures. In coarse-grained Al alloys, micro-alloying additions of Sc (<0.3 at.%) results in significant improvements in creep and coarsening resistance up

to 300 °C, due to the formation of nanoscale, elastically hard and coherent Al₃Sc(L1₂ structure) precipitates [1–10].

Many studies have identified elements that can substitute for Sc in Al–Sc-based alloys to: (i) decrease the use of the expensive Sc; (ii) increase ambient strength; (iii) increase service temperature, while maintaining high strength; and (iv) increase high-temperature creep strength. Substitutional elements for Sc are the rare-earth (RE) [11–23] and transition metals (TM) [24–36].

RE elements can substitute for Sc in L1₂-ordered Al₃(-Sc_{1-x}RE_x) precipitates, where x increases with the RE atomic mass and x is as large as 0.4 and can reach unity [14] for Er, Tm, Yb and Lu [15,37]. Diffusivities of RE elements in α -Al are essentially unknown, with the exception of Er and Yb. Their diffusivities at 300 °C were determined by measuring the kinetics of precipitation, and are

* Corresponding author at: Department of Materials Science and Engineering, Northwestern University, Evanston, IL 60208, USA. Tel.: +1 847 491 3575; fax: +1 847 491 7820.

E-mail address: voquynhon@gmail.com (N.Q. Vo).

four- and tenfold greater than Sc in α -Al, respectively [14]. Thereby, in dilute Al–Sc–Er and Al–Sc–Yb ternary alloys, the precipitate cores are enriched in Er and Yb, while their shells are enriched in Sc [13,19]. Similar observations were found for other RE elements (Sm, Gd, Tb, Dy, Ho, Tm and Lu) in Al–Sc–RE ternary alloys, where core–shell $\text{Al}_3(\text{Sc}_{1-x}\text{RE}_x)$ precipitates are found to be enriched in RE elements in their cores after aging at 300 °C [11,15,19]. As a result, RE substitution reduces the use of Sc, while maintaining the high number density of precipitates and thus the high ambient strength of an alloy. The high-temperature creep resistance of Al–Sc–RE ternary alloys is also improved compared with Al–Sc binary alloys [19,38–40], which is due to a larger lattice parameter mismatch between α -Al and $\text{Al}_3(\text{Sc}_{1-x}\text{RE}_x)$ [37], which increases the elastic interaction between precipitates and dislocations. Since RE elements appear to have larger diffusivities compared with Sc in α -Al, they do not improve precipitate coarsening resistance at higher service temperatures or longer exposure times.

Transition metals, such as Zr, Hf and Ti, can also substitute for Sc in L_{12} -ordered $\text{Al}_3(\text{Sc}_{1-x}\text{TM}_x)$ precipitates [24]. In the case of Zr, $\text{Al}_3(\text{Sc}_{1-x}\text{Zr}_x)$ precipitates exhibit significantly higher coarsening resistance compared with Al_3Sc precipitates in Al–Sc binary alloys, owing to the sluggish diffusivity of Zr in α -Al. A Zr-enriched precipitate shell is formed during aging and serves as a diffusion barrier for Sc, which is enriched in the precipitate core [31,28,29,41]. A recent study demonstrated that Al–0.06 Sc–0.06 Zr alloy maintains high strength at an aging temperature of 400 °C, with the average precipitate radius $\langle R(t) \rangle$ remaining nearly unchanged during aging for up to 64 days [41]. Titanium and Hf also improve the coarsening resistance of $\text{Al}_3(\text{Sc}_{1-x}\text{Ti/Hf}_x)$ precipitates by the same mechanism, but are less effective than Zr [27,30,42].

A combined approach to using the benefits of both RE and TM elements, where they substitute for Sc, has been achieved by designing new Al–Sc–Er–Zr alloys [41,43]. Alloy compositions and heat-treatment conditions were chosen, following the principal design requirements: affordability, high-temperature strength and coarsening resistance, maintaining precipitate coherence and minimizing grain refinement to eliminate diffusional creep. In Al–Sc–Zr alloys, research demonstrates that a total solute concentration below ~ 0.15 at.% results in larger grains in the as-cast condition by forming single α -Al phase alloys [29,31,32]. Thus, Sc and Zr concentrations of 0.06 at.% each were chosen to provide significant precipitation strengthening and sufficient coarsening resistance. With a solubility of 0.046 at.% Er in an Al–Er binary alloy at 640 °C [14], an Er concentration of < 0.02 at.% was chosen to reduce the occurrence of primary precipitates. As a result, coherent, spheroidal and L_{12} -ordered precipitates were formed, consisting of an Er-enriched core enveloped by a Sc-enriched inner shell and a Zr-enriched outer shell. The formation of nanostructured core/double-shell precipitate is a consequence of sequential precipitation according

to their intrinsic diffusivities ($D_{\text{Er}} > D_{\text{Sc}} > D_{\text{Zr}}$). The nanostructured precipitates are coarsening resistant for at least 64 days at 400 °C [41]. Moreover, substituting 0.01 at.% Er for Sc in the Al–0.06Sc–0.06Zr–0.04Si (at.%) alloy provides a significant improvement in the creep threshold stress, owing to an increase in the lattice mismatch between the $\text{Al}_3(\text{Sc,Zr,Er})$ precipitates and the α -Al matrix, compared with Er-free alloys [43].

The previous design and results for an Al–0.06Sc–0.06Zr at.% with 0.01 or 0.02 at.% Er substituting for Sc have several problems. The maximum solubilities of Er and Zr in the α -Al matrix are only ~ 50 and ~ 200 –300 at.ppm at 640 °C, respectively, as measured by atom-probe tomography (APT), owing to the formation of primary $\text{Al}_3\text{Er}(\text{L}_{12})$ and $\text{Al}_3\text{Zr}(\text{L}_{12})$ precipitates during solidification and subsequent cooling, and incomplete dissolution of the Al–Zr master alloy [41]. As a consequence, the Er-containing alloy had finer grains than the Er-free alloy, resulting in undesirable diffusional creep in the low-stress regime during creep experiments at 400 °C [43]. Substitution of 0.01 or 0.02 at.% Er for Sc resulted in a ~ 20 –30% decrease in microhardness, as a result of a smaller total Sc plus Er supersaturation [41]. Also, the heat treatment of the alloys was time consuming: 72 h for solutionizing/homogenizing at 640 °C and 24 h for peak-aging at 300 °C [43]. This article presents a further optimization of this advanced Al–Sc–Er–Zr alloy by decreasing the Er and Zr concentrations to 50 and 200 at.ppm, respectively, which are the experimentally measured maximum solubility values. A Sc concentration of 550 at.ppm was chosen, so that the total Sc + Er concentration is 0.06 at.% to regain the high ambient peak strength, and the total Sc + Er + Zr concentration is 0.08 at.% to prevent primary precipitation during solidification, and to maintain a coarse-grained structure that does not exhibit measurable diffusional creep at small stresses. Decreasing the concentrations of the relatively expensive Er and Zr also results in less expensive alloys. Furthermore, 0.05 at.% Si was added to obtain three important advantages: (i) increasing precipitate number density by stimulating heterogeneous nucleation [44]; (ii) accelerating the Er and Sc precipitation kinetics to decrease the aging time [44]; and (iii) decreasing the cost of the alloy because of the presence of Si impurities in commercial-purity aluminum [45].

2. Experimental procedures

The alloy with a nominal composition of Al–0.055Sc–0.005Er–0.02Zr–0.05Si (at.%) (which is used hereafter unless noted otherwise), referred to as the improved alloy, was melted in air in a resistively heated furnace using 99.999 at.% pure Al, Al–12Si, Al–5.0Zr, Al–1.3Sc and Al–1.2Er, in alumina crucibles. The master alloys were preheated to 640 °C to accelerate solute dissolution upon addition to the melt. The melt was held for 30 min at 800 °C, stirred vigorously and then cast into a graphite mold, which was preheated to 200 °C. The mold was placed on

an ice-cooled copper platen during solidification to enhance directional solidification and decrease the formation of shrinkage cavities. The alloy's chemical composition was measured by direct-current plasma atomic-emission spectroscopy (DCP-AES) at ATI Wah Chang (Albany, OR) and by APT (Table 1).

The cast alloy was homogenized in air at 640 °C for times ranging from 0.08 to 72 h, then water quenched to ambient temperature. Two aging heat treatments were conducted: (i) isochronal aging in 1 h steps of 25 °C for temperatures ranging from 100 to 475 °C; and (ii) isothermal aging at temperatures from 300 to 450 °C for times up to 125 days. All heat treatments were conducted in air and terminated by water quenching to ambient temperature.

Vickers microhardness measurements were performed with a Duramin-5 microhardness tester (Struers) using a 200 g load applied for 5 s on samples polished to a 1 μm surface finish. At least ten indentations across different grains were made per specimen. Electrical conductivity measurements were performed using a Sigmatest 2.069 eddy current instrument (Foerster Instruments, Pittsburgh, PA). Five measurements at 120, 240, 480 and 960 kHz were performed per specimen. Primary precipitates on the polished and unetched surface were imaged by scanning electron microscopy (SEM) using a Hitachi S-4800-II microscope equipped with an Oxford INCAx-act detector for energy-dispersive X-ray spectroscopy.

Specimens for three-dimensional (3-D) local-electrode atom-probe (LEAP) tomography were prepared by cutting blanks with a diamond saw to $\sim 0.35 \times 0.35 \times 10 \text{ mm}^3$. These samples were then electropolished at 20–25 V DC, using a solution of 10% perchloric acid in acetic acid, followed by electropolishing at 12–18 V DC employing a solution of 2% perchloric acid in butoxyethanol: both were performed at room temperature. Pulsed-laser APT was performed using a LEAP 4000X Si-X tomograph (Cameca, Madison, WI) [46,47] at a specimen temperature of 30 K. For pulsed-laser dissection, a focused picosecond ultraviolet (UV) laser pulse (wavelength = 355 nm) with a laser beam waist of $< 5 \mu\text{m}$ at the e^{-2} diameter was used. An UV laser energy of 80 pJ pulse^{-1} , and a pulse repetition rate of 500 kHz were used. LEAP tomographic data were analyzed employing IVAS version 3.6.1 (Cameca). The measurement errors for all quantities were calculated based on counting statistics and standard error propagation techniques [48].

3. Results

3.1. Minimization of homogenization time

The as-cast improved alloy was homogenized at 640 °C for different times, ranging from 0 to 72 h. Electrical conductivity as a function of homogenization time (Fig. 1) initially decreases from $32.31 \pm 0.07 \text{ MS m}^{-1}$ as homogenization time increases and then saturates at $\sim 31.7 \text{ MS m}^{-1}$ after 1 h. SEM micrographs of the as-cast state (Fig. 2a)

display Er-enriched primary precipitates, which appear to almost fully dissolve after 2 h of homogenization (Fig. 2b). The disappearance of Er-enriched precipitates results in a coarse grain structure, $0.3 \pm 0.1 \text{ grain mm}^{-2}$, for the improved alloy, double-aged at 300 °C for 4 h and 425 °C for 8 h, after a 2 h homogenization (Fig. 2c). Therefore, the initial decrease in electrical conductivity for a short homogenization time is probably the result of the dissolution of the Al_3Er primary precipitates. A number density of primary Al_3Er precipitates of $\sim 4 \times 10^{14} \text{ m}^{-3}$ with radii of a few micrometers in the as-cast state is unexpected, since Er is present only at one-tenth (0.005 at.%) of the maximum Er solubility in an Al–Er binary alloy (0.046 at.%) at 640 °C [14]. Erbium may be enriched locally because of segregation occurring during casting, causing primary precipitation.

The Vickers microhardness of the improved alloy, homogenized at 640 °C for different times and subsequently aged at 400 °C for 4 h, which is close to the peak-aging condition [41], is displayed in Fig. 1. The microhardness increases initially from $\sim 360 \text{ MPa}$ with increasing aging time and saturates at $\sim 520 \text{ MPa}$ after 0.3 h. This trend is similar to the evolution of the electrical conductivity. Prior research showed that, in the absence of Er, a small number density of non-equilibrium precipitates is formed during aging at 400 °C, resulting in a microhardness of only $\sim 225 \text{ MPa}$ after 4 h of aging in an Al–0.06Sc–0.06Zr alloy

Table 1

Composition (at.%) of the alloy studied, as measured by DCP-AES and LEAP tomography; measurement uncertainty is given in parenthesis after the significant digit to which it applies.

	Si	Sc	Zr	Er
Nominal	0.050	0.055	0.020	0.005
DCPMS	0.044	0.056	0.021	0.007
LEAP	0.0401(6) ^a	0.0530(7)	0.0143(4)	0.0039(2)

^a Atomic concentration of $^{28}\text{Si}^{2+}$ ions in LEAP tomographic mass spectrum.

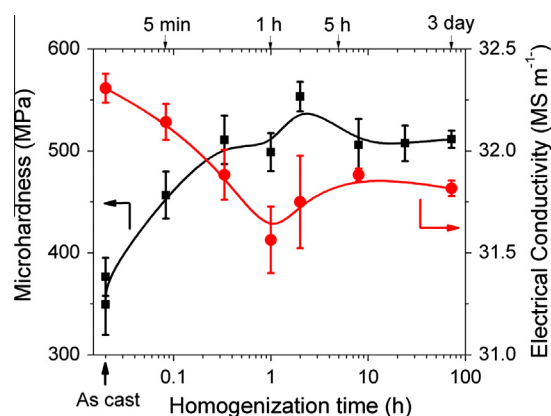


Fig. 1. Electrical conductivity of Al–0.055Sc–0.005Er–0.02Zr–0.05Si (improved alloy) homogenized at 640 °C for different times (red) and Vicker microhardness of improved alloy homogenized at 640 °C for different times, then aged at 400 °C for 4 h (black). (For interpretation of the references to color in this figure legend, the reader is referred to the web version of this article.)

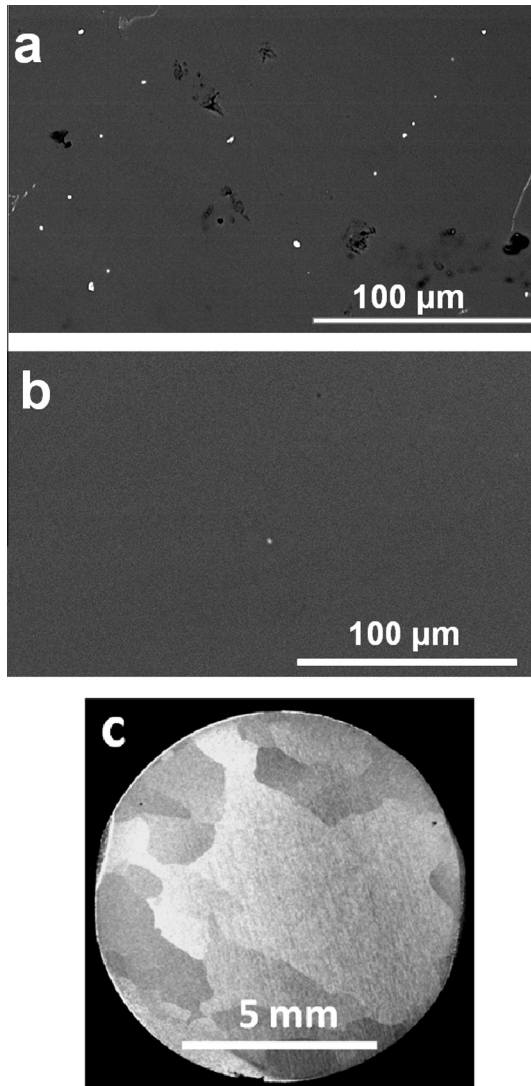


Fig. 2. SEM micrograph of Al-0.055Sc-0.005Er-0.02Zr-0.05Si (improved alloy) (a) in as-cast state, showing Al_3Er primary precipitates, and (b) homogenized at 640 °C for 2 h, exhibit no sign of Al_3Er primary precipitates. (c) Coarse grain structure of improved alloy ($\sim 0.3 \pm 0.1$ grain mm^{-2}), homogenized at 640 °C for 2 h, then double aged at 300 °C for 4 h and 425 °C for 8 h.

[41]. The microhardness of the as-cast improved alloy is 360 MPa after 4 h of aging at 400 °C, suggesting that a small Er supersaturation is available in the α -Al phase, despite the formation of primary precipitates. Alternatively, the presence of Si could also increase the microhardness by promoting heterogeneous nucleation of precipitates during aging at 400 °C. After being homogenized for at least 0.3 h at 640 °C, primary Al_3Er precipitates were fully dissolved, increasing the Er supersaturation during subsequent aging at lower temperatures, hence increasing the microhardness of the aged improved alloy. Beyond dissolution of primary precipitates, homogenization also reduces solute gradients created during solidification of the alloy. How this homogenization process and the existence of Si affect the microhardness after homogenization

is beyond the scope of this investigation. Based on these results, all the alloys studied herein were homogenized for at least 2 h at 640 °C before further heat treatment. This represents a 36-fold reduction in homogenization time compared with the previously used value of 72 h [11,15,41,43], which is critical for cost-effective processing of these alloys.

3.2. Isochronal aging

The evolution of the Vickers microhardness and electrical conductivity during isochronal aging in 1 h steps of 25 °C is displayed in Fig. 3 for the as-cast and 2 h homogenized improved alloy. Data for the quaternary Al-0.05Sc-0.01Er-0.06Zr alloy homogenized for 72 h [41] are presented for comparison. In the latter alloy, precipitation commences at 200 °C. The microhardness increases from 229 ± 4 to 311 ± 9 MPa at 275 °C before increasing rapidly at higher temperatures. The first rise below 275 °C should correspond to Er precipitation, because Er is a faster diffuser than Sc or Zr. The peak microhardness value of 488 ± 18 MPa at 325 °C should correspond to precipitation of Sc, while Zr is precipitating mainly during the microhardness plateau (~ 475 MPa) between 350 and 450 °C. The electrical conductivity increases slightly from

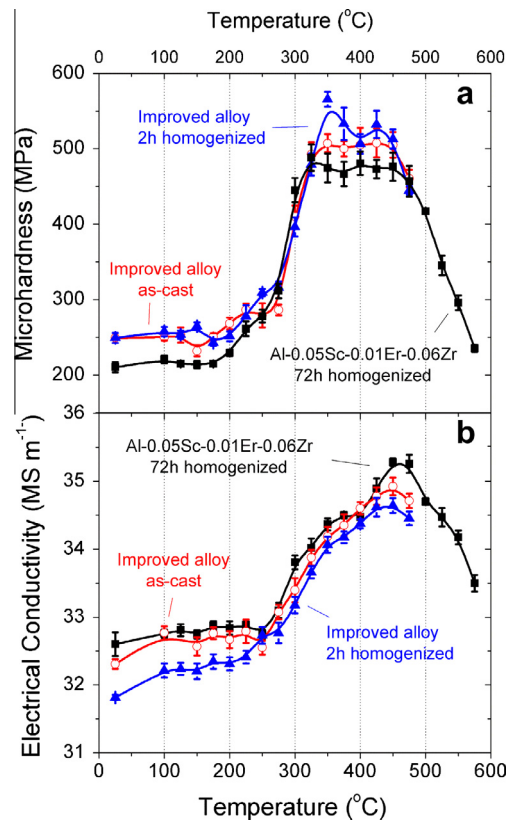


Fig. 3. Evolution of Vickers microhardness and electrical conductivity during isochronal aging (25 °C for 1 h) for Al-0.05Sc-0.01Er-0.06Zr, homogenized at 640 °C for 72 h [41], and Al-0.055Sc-0.005Er-0.02Zr-0.05Si (improved alloy) in as-cast state and homogenized at 640 °C for 2 h.

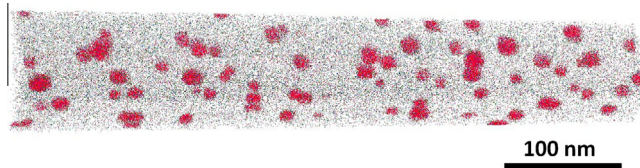


Fig. 4. APT reconstruction of Al-0.055Sc-0.005Er-0.02Zr-0.05Si (improved alloy) aged isochronally to 450 °C, after being homogenized at 640 °C for 2 h, showing nano-precipitates. Sc atoms are displayed in red, Zr atoms are in green, Er atoms are in blue, Si atoms are in black, and Al atoms are omitted for clarity. (For interpretation of the references to color in this figure legend, the reader is referred to the web version of this article.)

100 to 275 °C, before rapidly increasing and peaking at 450 °C, achieving $35.28 \pm 0.06 \text{ MS m}^{-1}$. Above 450 °C, both microhardness and electrical conductivity continuously decrease as a result of the dissolution of precipitates.

In the improved alloy, both as-cast and 2 h homogenized states behave similarly to the quaternary Al-0.05Sc-0.01Er-0.06Zr alloy homogenized for 72 h at 640 °C. The as-cast alloy displays earlier precipitation of Er in the range 200–275 °C, suggesting that Er is still supersaturated after solidification, despite the formation of primary Al_3Er precipitates. A microhardness peak of $507 \pm 12 \text{ MPa}$ is achieved at 350 °C, mainly as a result of Sc precipitation, followed by a $\sim 505 \text{ MPa}$ plateau from 350 to 450 °C when Zr precipitates. In the homogenized improved alloy, the microhardness of $566 \pm 10 \text{ MPa}$ peaks at 350 °C, which is an $\sim 80 \text{ MPa}$ increase compared with the Al-0.05Sc-0.01Er-0.06Zr alloy. The microhardness then decreases before peaking for a second time at 425 °C at a value of $532 \pm 18 \text{ MPa}$. Again, the first and second peaks are attributed to the precipitation of Sc and Zr, respectively. These results are consistent with previous studies of Al-0.1Sc-0.1Zr [31] and Al-0.06Sc-0.06Zr [32] alloys. The electrical conductivity trends for the as-cast and homogenized improved alloys are similar to those of the Al-0.05Sc-0.01Er-0.06Zr alloy. Above 450 °C, continuous decreases in microhardness and electrical conductivity are observed owing to dissolution of precipitates. Based on these observations, an addition of 0.05 at.% Si in the improved alloys does not significantly alter the isochronal aging behavior of the quaternary Al-0.05Sc-0.01Er-0.06Zr alloy, except for an increase in peak microhardness from 488 to 566 MPa. The alloy homogenized for 2 h also exhibits somewhat higher microhardness values compared with the as-cast alloy during isochronal aging.

The microstructure of the nano-precipitates in the improved alloy, homogenized for 2 h at 640 °C and then isochronally aged to 450 °C, is displayed in Fig. 4. The precipitate number density N_v is $1.6 \pm 0.2 \times 10^{22} \text{ m}^{-3}$, and their average radius and volume fraction are $3.0 \pm 0.7 \text{ nm}$ and 0.185%, respectively (Table 2). For comparison, the unimproved Al-0.04Sc-0.02Er-0.06Zr alloy has $N_v = 0.86 \pm 0.15 \times 10^{22} \text{ m}^{-3}$, $\langle R \rangle = 3.4 \pm 0.6 \text{ nm}$ and $\phi = 0.157\%$. The improved alloy has larger values of N_v and ϕ , while $\langle R \rangle$ is smaller. The differences between the two alloys are attributed to the smaller matrix solute supersaturation caused by the primary precipitation of Er during solidification of the Al-0.04Sc-0.02Er-0.06Zr alloy. Alternatively, addition of 0.05 at.% Si could also increase N_v , concomitantly decreasing $\langle R \rangle$, by inducing heterogeneous nucleation of $\text{Al}_3(\text{Sc,Zr,Er})$ precipitates. This possibility is discussed in Section 4.4.2.

Fig. 5 displays a proximity histogram [49], which exhibits the average concentrations in shells 0.25 nm thick at a given distance from the average $\alpha\text{-Al}/\text{Al}_3\text{Sc}$ interface defined by an isoconcentration surface at the inflection point of the Al concentration profile. Erbium and Si are homogeneously distributed in the precipitates, while Zr is enriched and Sc is depleted in an outer shell $\sim 0.5 \text{ nm}$ thick. The average precipitate composition is 70.30 Al, 1.71 Si, 25.11 Sc, 1.35 Zr and 1.53 Er at.% (Table 3). The precipitate core consists of a mixture of Sc, Er and Si, suggesting that these elements co-precipitated during the early stage of the heat treatment. This is surprising, since Er diffuses faster than Sc in binary Al–Er and Al–Sc alloys [14]. Precipitates in Al–Sc–Er–Zr alloys exhibit an Er-enriched core, a Sc-enriched inner shell and a Zr-enriched outer shell, a layered structure explained by the sequential precipitation of the three elements according to the values of their intrinsic diffusivities in Al [41]. Addition of 0.05 at.% Si is therefore strongly modifying the precipitation kinetics of Er and Sc.

3.3. Isothermal aging at 400 °C

The evolution of the Vickers microhardness and electrical conductivity in the improved alloy during isothermal aging at 400 °C up to 125 days (3000 h), homogenized for 72 h, are displayed in Fig. 6a and b, respectively. Data for Al-0.05Sc-0.01Er-0.06Zr and Al-0.04Sc-0.02Er-0.06Zr alloys without silicon [41] are plotted for comparison. The Vickers microhardness values of these two Si-free alloys are comparable over the entire aging time. It

Table 2

Precipitate number density N_v , average radius $\langle R \rangle$, volume fraction ϕ and microhardness HV for Al-0.055Sc-0.005Er-0.02Zr-0.05Si (improved alloy) aged isochronally to 450 °C after being homogenized at 640 °C for 2 h, or isothermally at 400 °C for 0.5 and 66 days after being homogenized at 640 °C for 72 h.

Alloys	$N_v (\times 10^{22} \text{ m}^{-3})$	$\langle R \rangle (\text{nm})$	$\phi (\%)$	HV (MPa)
Isochronal to 450 °C	1.59 ± 0.20	3.0 ± 0.7	0.185	513 ± 13
Isothermal at 400 °C for 0.5 h	1.11 ± 0.37	4.1 ± 0.8	0.235	504 ± 13
Isothermal at 400 °C for 66 days	0.20 ± 0.10	6.3 ± 0.3	0.210	429 ± 14

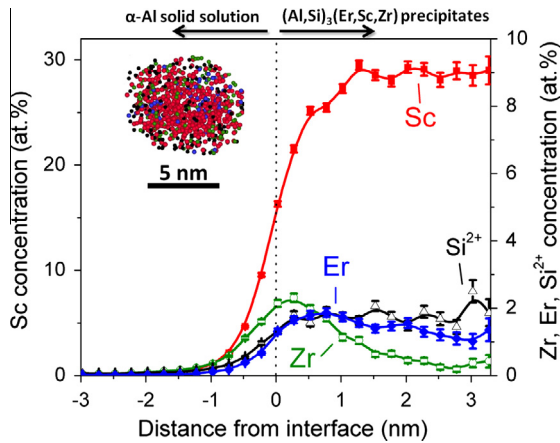


Fig. 5. Concentration profiles across the matrix/precipitate interface of Al-0.055Sc-0.005Er-0.02Zr-0.05Si (improved alloy) isochronally aged to 450 °C, after being homogenized at 640 °C for 2 h (Fig. 4). The inset image is the APT reconstruction of a representative precipitate from the alloy. Sc atoms are displayed in red, Zr atoms are in green, Er atoms are in blue, Si atoms are in black, and Al atoms are omitted for clarity. (For interpretation of the references to color in this figure legend, the reader is referred to the web version of this article.)

increases slightly up to 0.2 h of aging and then dramatically increases to ~ 420 MPa at 0.5 h. The Vickers microhardness then gradually increases and peaks at ~ 460 MPa after 12 days' aging, before diminishing slightly up to day 256 of aging, as a result of precipitate coarsening. The electrical conductivity of the two Si-free alloys increases steadily up to ~ 2 days of aging, indicating continuous precipitation (Fig. 6b). It achieves a plateau between day 2 and day 64 of aging, suggesting that the majority of the solute atoms have precipitated. The electrical conductivity increases slightly beyond day 64 of aging as the matrix concentrations evolve toward their thermodynamic equilibrium values and the precipitates coarsen.

The evolution of the Vickers microhardness in the improved Si-containing alloy displays several distinct differences compared with the Si-free alloys (Fig. 6a). The rapid increase in microhardness occurs earlier than in the Si-free alloys; after only 0.2 h aging, a significantly higher microhardness plateau of 493 ± 10 MPa is achieved. The microhardness peaks at 533 ± 12 MPa after 60 h of aging, before continuously diminishing with increasing aging time. The electrical conductivity in the improved alloy increases steadily up to day 2 of aging (Fig. 6b), with an abrupt increase (from 32.2 to 34.2 MS m^{-1}) in the range

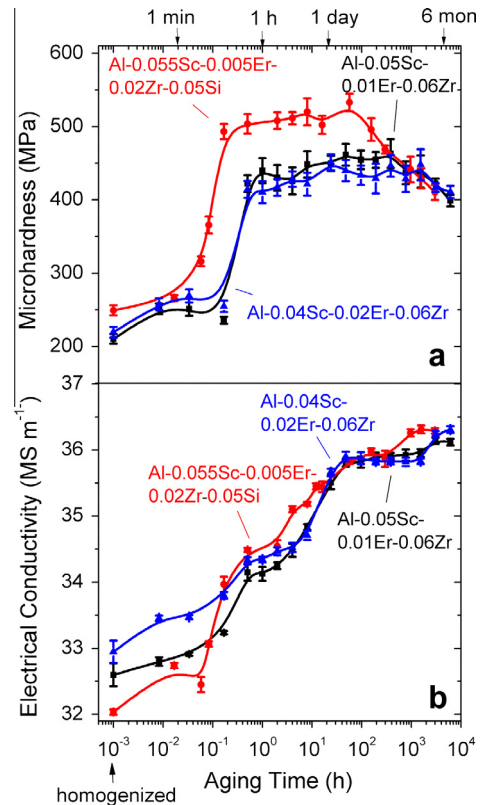


Fig. 6. Evolution of Vickers microhardness and electrical conductivity during isothermal aging at 400 °C for Al-0.05Sc-0.01Er-0.06Zr [41], Al-0.04Sc-0.02Er-0.06Zr [41] and Al-0.055Sc-0.005Er-0.02Zr-0.05Si (improved alloy), after being homogenized at 640 °C for 72 h.

0.06–0.5 h of aging. The abrupt increase in electrical conductivity, coinciding with a rapid increase in microhardness, suggests that the precipitation kinetics of Er and Sc are accelerated by the addition of Si.

The chemical compositions of the nanosize precipitates of the improved alloy aged isothermally for 0.5 h and 66 days are compared using APT reconstructions (Fig. 7) and associated concentration profiles (Fig. 8). After 0.5 h of aging, the improved alloy has $N_v = 1.11 \pm 0.37 \times 10^{22} \text{ m}^{-3}$, $\langle R \rangle = 4.1 \pm 0.8$ nm and $\phi = 0.235\%$. The average precipitate composition is 73.35Al, 2.75Si, 21.38Sc, 0.30Zr and 2.22Er at.% (Table 3). The precipitates display a homogenized mixture of Sc, Er and Si, surrounded by a shell slightly enriched in Zr (Fig. 8a). The following possible scenario is likely: Sc, Er and Si co-precipitate at an early

Table 3

Composition of precipitates and matrix in Al-0.055Sc-0.005Er-0.02Zr-0.05Si (improved alloy) aged isochronally to 450 °C after being homogenized at 640 °C for 2 h, or isothermally at 400 °C for 0.5 and 66 days after being homogenized at 640 °C for 72 h.

Alloys	Precipitate composition (at.%)					Matrix composition (at.ppm)			
	Al	Si ^a	Sc	Zr	Er	Si ^a	Sc	Zr	Er
Isochronal to 450 °C	70.30(13)	1.71(4)	25.11(12)	1.35(3)	1.53(4)	396(2)	165(1)	77(1)	4(2)
Isothermal at 400 °C for 0.5 h	73.35(21)	2.75(8)	21.38(20)	0.30(3)	2.22(7)	274(3)	76(2)	157(3)	21(9)
Isothermal at 400 °C for 66 days	74.17(13)	1.13(3)	19.53(12)	3.46(6)	1.71(4)	441(7)	49(2)	14(1)	14(1)

^a Atomic concentration of $^{28}\text{Si}^{2+}$ ions in LEAP tomographic mass spectrum.

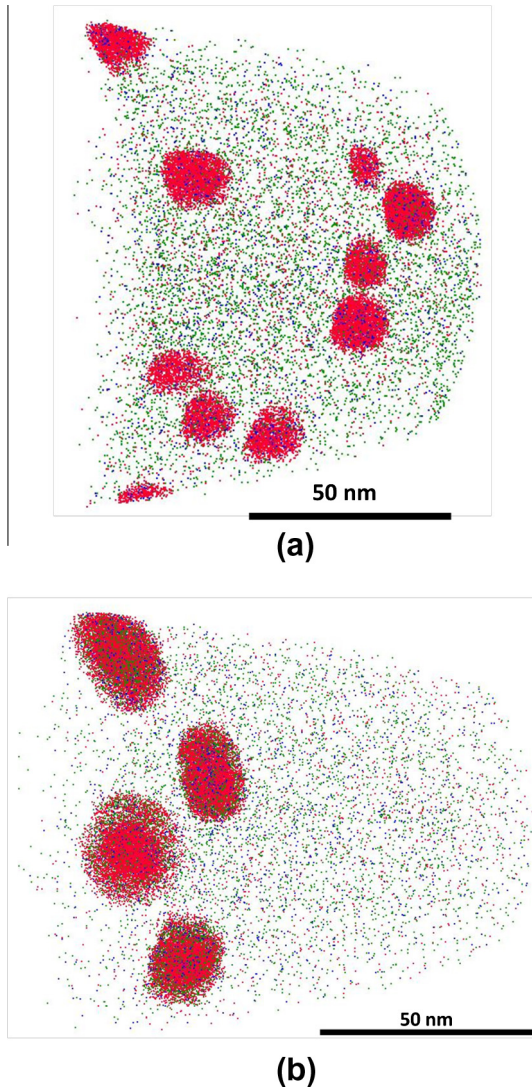


Fig. 7. APT reconstruction of Al-0.055Sc-0.005Er-0.02Zr-0.05Si (improved alloy) aged isothermally at 400 °C for (a) 0.5 h and (b) 66 days, after being homogenized at 640 °C for 72 h, showing nano-precipitates. Sc atoms are displayed in red, Zr atoms are in green, Er atoms are in blue, Si atoms are in black, and Al atoms are omitted for clarity. (For interpretation of the references to color in this figure legend, the reader is referred to the web version of this article.)

stage of aging, while Zr precipitates at a later stage. Formation of the Zr-enriched shell is surprising, because the root-mean-square (RMS) diffusion distance ($\sqrt{4Dt}$) of Zr in pure Al [50] at 400 °C for 0.5 h is 9 nm, which is less than the estimated edge-to-edge inter-precipitate distance of 77 nm.

After 66 days of aging, the improved alloy has $N_v = 0.20 \pm 0.10 \times 10^{22} \text{ m}^{-3}$, $\langle R \rangle = 6.3 \pm 0.3 \text{ nm}$ and $\phi = 0.210\%$. The alloy appears to be in the coarsening stage, as ϕ is nearly constant, N_v decreases fourfold, and $\langle R \rangle$ increases by a factor 1.5 compared with the alloy aged for 0.5 h. A signature of coarsening of the precipitates is visible in the precipitate concentration profile (Fig. 8b) in the form of an outer shell with higher Zr and lower Er

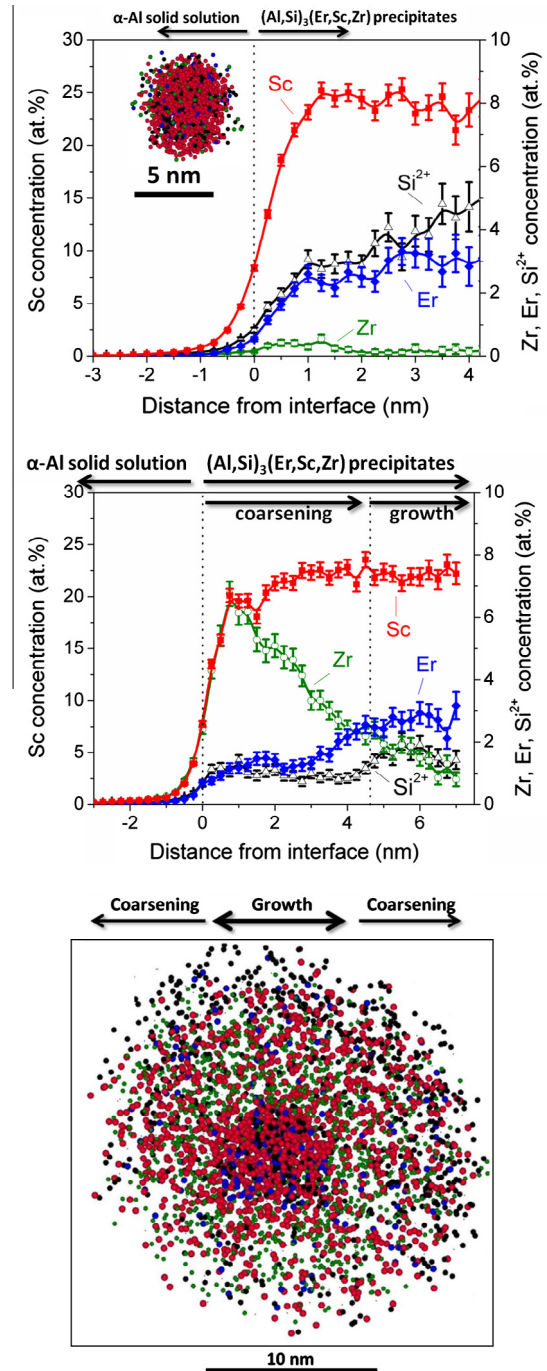


Fig. 8. Concentration profiles across the matrix/precipitate interface of Al-0.055Sc-0.005Er-0.02Zr-0.05Si (improved alloy) isothermally at 400 °C for (a) 0.5 h and (b) 66 days, after being homogenized at 640 °C for 72 h (Fig. 7). The inset image in (a) and image (c) show the APT reconstruction of a representative precipitate from the alloy. Sc atoms are displayed in red, Zr atoms are in green, Er atoms are in blue, Si atoms are in black, and Al atoms are omitted for clarity. (For interpretation of the references to color in this figure legend, the reader is referred to the web version of this article.)

and Si concentrations than the inner core. The inner core, with a 2–3 nm radius corresponding to 2–8% of the precipitates' volume, consists of 71.80Al, 1.63Si, 22.11Sc, 1.50Zr and 2.65Er at.%. The outer shell has a composition of 72.93Al, 1.01Si, 20.11Sc, 3.98Zr and 1.55Er at.%. The

present authors interpret the precipitates' inner core composition to represent the precipitates created in the initial nucleation process and early growth stage. This is because the average composition and composition gradients within the inner core agree with those of precipitates in the alloy aged for 0.5 h (Fig. 8a). The outer shell is the result of subsequent coarsening, and contains significantly more of the slow diffusing Zr. The RMS diffusion distance of Zr in pure Al [50] at 400 °C at day 66 is 517 nm. Fig. 8c presents the 3-D nanostructure of a representative precipitate complementing the concentration profiles (Fig. 8b).

3.4. Isothermal aging at temperatures ranging from 300 to 450 °C

The Vickers microhardness and electrical conductivity evolve in the improved alloy, during isothermal aging at 300, 425 and 450 °C up to 125 days (3000 h) after 2 h homogenization and 400 °C after 72 h homogenization (Fig. 9a and b, respectively). At 300 °C, the microhardness (Fig. 9a) increases slightly from 249 ± 7 MPa in the homogenized state to 297 ± 5 MPa after 0.2 h of aging, before rapidly increasing to 492 ± 11 MPa after 1 h of aging. The microhardness increases continuously at longer aging times and is still increasing at the longest aging time of 1008 h, achieving a value of 606 ± 22 MPa. The electrical conductivity increases steadily up to 1 h of aging, indicating continuous precipitation (Fig. 9b). It achieves a plateau between 1 and 16 h of aging, before increasing con-

tinuously up to the longest aging time of 1008 h. The plateau may indicate nearly completed precipitation of Er and Sc, while the further increases suggest that Zr segregate to the interface of $\text{Al}_3(\text{Sc,Zr,Er})$ precipitates. The latter increases the precipitate volume fraction, while possibly maintaining a constant value of N_v , which causes a corresponding increase in microhardness. It also suggests that the microhardness may achieve a higher value, because Zr has not completely segregated at the longest aging time of 1008 h (day 42).

At 425 °C the microhardness (Fig. 9a) increases slightly from 249 ± 7 MPa in the homogenized state to 265 ± 4 MPa after 0.02 h of aging, before increasing rapidly and peaking at 515 ± 16 MPa after aging for 8 h. It then decreases continuously at longer aging times and achieves a value of 305 ± 7 MPa after 3000 h of aging, which is 105 ± 12 MPa lower than at 400 °C for the same aging time. The evolution of the electrical conductivity (Fig. 9b) is, however, similar to the aging at 400 °C up to the longest aging time, suggesting that rapid precipitate coarsening is occurring during aging at 425 °C.

At 450 °C, the microhardness (Fig. 9a) peaks at 459 ± 8 MPa after 0.6 h of aging (or possibly earlier, as this was the earliest time measured) and remains constant to 27 h, before declining continuously to 343 ± 11 MPa after 520 h of aging. The electrical conductivity increases from 31.82 ± 0.04 MS m^{-1} in the homogenized state to 34.10 ± 0.04 MS m^{-1} after 0.6 h of aging, before increasing steadily to 35.22 ± 0.05 MS m^{-1} at the longest aging time of 520 h. The electrical conductivity curve at 450 °C appears near saturation at a shorter time than at 400 and 425 °C, which is most likely caused by a higher equilibrium solute solubility and more rapid precipitate coarsening at 450 °C. In conclusion, higher peak microhardness and improved coarsening resistance can be achieved at 300 °C, while the opposite effects occur at aging temperatures of 400–450 °C.

4. Discussion

4.1. Homogenization heat treatment

Homogenization/solutionization, performed at 640 °C for the improved alloy, aims to eliminate solute microsegregation and dissolve primary precipitates formed during solidification. Microsegregation was reported in Al–0.06Sc, Al–0.06Zr, Al–0.06Sc–0.06Zr and Al–0.1Sc–0.1Zr [31,32]. Al_3Er , Al_3Sc and Al_3Zr primary precipitates can also form during solidification [51]. The SEM micrograph in Fig. 2a reveals, however, only Er-enriched precipitates. Er has a larger diffusivity than Sc and Zr [14], and it tends to precipitate during quenching from the melt, in part because of its small solubility in $\alpha\text{-Al}$. SEM microscopy (Fig. 2b) indicates that full dissolution of the $\text{Al}_3\text{Er}(\text{L}1_2)$ primary precipitates occurs after homogenization for 2 h at 640 °C. A decrease in electrical conductivity of 0.6 MS m^{-1} corresponds to an increase in electrical

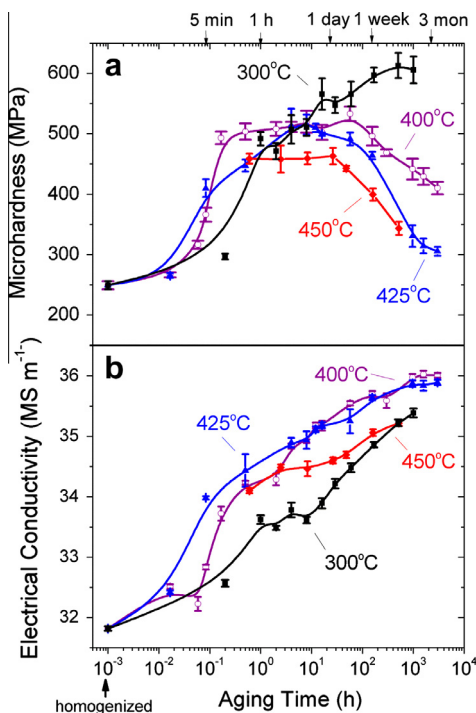


Fig. 9. Evolution of Vickers microhardness and electrical conductivity during isothermal aging at 300, 425 and 450 °C after being homogenized at 640 °C for 2 h, and at 400 °C after being homogenized at 640 °C for 72 h, for Al–0.055Sc–0.005Er–0.02Zr–0.05Si (improved alloy).

resistivity ρ of 0.6 p Ω m. If one assumes that this is completely due to the dissolution of Al₃Er in the α -Al matrix, and the coefficient $\Delta\rho/c$ (where c is atomic concentration) for Er is 0.05 $\mu\Omega$ m (at.%)⁻¹ [23], it yields an Er concentration of 0.012 at.%, which is in reasonable agreement with the nominal Er concentration of 0.005 at.%. In conclusion, homogenization is necessary for the improved alloy to dissolve the Al₃Er primary precipitates, thereby maximizing the Er supersaturation and preventing grain boundary pinning by Al₃Er precipitates, which prevents the alloy from achieving the coarse grain structure required for excellent creep resistance. A short aging time of 0.5–2 h is sufficient, which is less than the 72 h used in previous studies, where homogenization of the slow diffusing Zr was also desired. It is noteworthy that the grain number density obtained in the improved alloys, homogenized for 2 h, double-aged at 300 °C for 4 h and 425 °C for 8 h, 0.3 ± 0.1 grain mm⁻², is about an order of magnitude smaller than in the Al–0.05Sc–0.01Er–0.06Zr–0.04Si alloy, 2.1 ± 0.2 grain mm⁻², after a similar age-hardening heat treatment, following homogenization at 640 °C for 72 h [43].

4.2. Strengthening mechanisms

The equations for the different mechanisms causing precipitation strengthening [15,41,43] are given in the Appendix: ordering strengthening σ_{ord} , coherence and modulus strengthening, $\sigma_{coh} + \sigma_{mod}$, and Orowan dislocation looping strengthening σ_{Or} . The calculated strengthening of the improved alloy, where APT data are used as input parameters, are presented in Table 4 and compared with the measured strengthening increment, estimated as $\Delta HV/3$, where ΔHV is the microhardness increase from the base microhardness of 200 MPa of the precipitate-free Al alloy [11,15,32] to the microhardness in the aged state. In the improved alloy aged isochronally to 450 °C with $\langle R \rangle = 3.0$ nm, the measured strengthening increment of 104 ± 5 MPa is slightly higher than the calculated Orowan dislocation looping value of 97 ± 9 MPa, and calculated ordering strengthening value of 101 MPa, and much lower than the coherence and modulus strengthening value of 148 MPa. $\langle R \rangle$ is in the critical range 2.0–4.0 nm, where the deformation mechanism changes from precipitate shearing to Orowan dislocation looping [3]. Therefore, a mixed strengthening mechanism may be operating, with some precipitates being sheared and others being bypassed. In the improved alloy aged isothermally at 400 °C for 0.5 h and 66 days, with $\langle R \rangle = 4.1 \pm 0.8$ and 6.3 ± 0.3 nm,

respectively, the measured strengthening increments are 101 ± 5 and 76 ± 5 MPa, respectively. These values are closest to the calculated Orowan dislocation looping strengthening values (89 ± 9 and 62 ± 2 MPa, respectively), and smaller than the strengths calculated for the other mechanisms (Table 4). It is therefore concluded that the Orowan bypass strengthening mechanism is operative in these two alloys, as was found for many other Al–Sc–X alloys for this range of $\langle R \rangle$ [3,15,41].

4.3. Improving the aging heat treatment

An improved aging heat treatment should result in both good strength and short aging times. A peak aging heat treatment of <8 h (a typical industrial work shift) is cost effective for processing these alloys. Fig. 9a reveals that a large microhardness value can be achieved after aging at 300 °C for 16 h, where a first microhardness plateau is reached. Compared with aging at higher temperatures, the maximum driving force for nucleation and sufficiently large intrinsic diffusivities for Er and Sc (Fig. 3) should achieve a maximum value for the precipitate number density. At longer aging times at 300 °C, the microhardness increases again, which is attributed to the slower diffusing Zr segregating to the interface of Al₃(Sc,Zr,Er) precipitates, thus increasing their total volume fraction. At the longest aging time of 1008 h (42 days) at 300 °C, the second peak in microhardness is achieved, despite the sluggish diffusivity of Zr atoms [41,50]. The diffusion distance of Zr in pure Al [50] at 300 °C for 1008 h is 9 nm, but it may be greater in the presence of Si, as discussed later. This prohibitively long aging treatment at 300 °C can be replaced by a much shorter two-step aging heat treatment. The first step involves aging at a low temperature to maximize the number density of nucleated precipitates, e.g., 1 h at 300 °C. The second step involves aging at a higher temperature, to maximize the precipitate's volume fraction at 375 to 400 °C for a few hours by segregating Zr to the interface of Al₃(Sc,Zr,Er) precipitates. This approach is demonstrated in Fig. 10. The improved alloy achieved 571 ± 11 MPa after a two-step aging at 300 °C for 1 h, then 375 °C for 2 h, the same microhardness value as achieved after aging at 300 °C for 16–70 h. Two-step aging at 300 °C for 1 h, then 400 °C for a few hours is not as effective, possibly because of the high solubility of solutes at 400 °C. The two-step aging treatment approach was also used successfully in previous research [41,43].

Table 4

Experimental ($\Delta HV/3$) and calculated strength increments (Eqs. (A1)–(A4)) of Al–0.055Sc–0.005Er–0.02Zr–0.05Si (improved alloy) aged isochronally to 450 °C after being homogenized at 640 °C for 2 h, or isothermally at 400 °C for 0.5 and 66 days after being homogenized at 640 °C for 72 h.

Alloys	$\Delta\sigma_{ord}$ (MPa) (Eq. (A1))	$\Delta\sigma_{coh} + \Delta\sigma_{mod}$ (MPa) (Eqs. (A2) and (A3))	$\Delta\sigma_{Or}$ (MPa) (Eq. (A4))	$\Delta HV/3$ (MPa)
Isochronal to 450 °C	101	148	97	104 ± 5
Isothermal at 400 °C for 0.5 h	114	186	89	101 ± 5
Isothermal at 400 °C for 66 days	108	204	62	76 ± 5

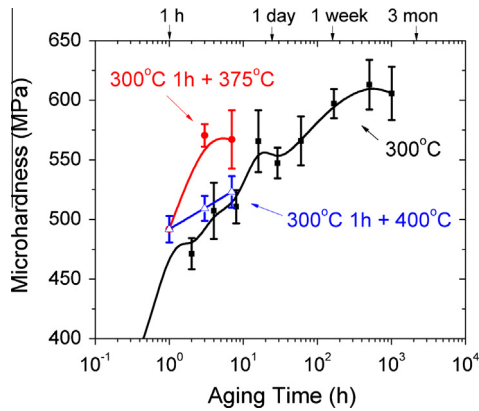


Fig. 10. Evolution of Vickers microhardness for Al-0.055Sc-0.005Er-0.02Zr-0.05Si (improved alloy) during isothermal aging at 300 °C, after being homogenized at 640 °C for 2 h. Double-aging at 300 °C for 1 h, then at either 375 or 400 °C for longer aging times is also displayed.

4.4. Effect of Si additions

4.4.1. Acceleration of precipitation kinetics

The reduction in the peak aging time from 30 min in the Si-free Al-0.05Sc-0.01Er-0.06Zr alloy [41] to 10 min for the Si-containing Al-0.055Sc-0.005Er-0.02Zr-0.05Si alloy at 400 °C (Fig. 6a) demonstrates that Si accelerates the precipitation kinetics. At this early stage of aging, Er and Sc are responsible for precipitation, and the RMS Zr diffusion distances are negligible. A recent study demonstrated how Si accelerates Sc precipitation kinetics in Al-0.06Sc-0.06Zr-0.06Si [44]. First-principles calculations of solute-solute binding energies of a Si-Sc dimer at the first and second nearest-neighbor distances yields positive (attractive) values of 0.33 and 0.13 eV pair⁻¹, respectively. They also reveal that a vacancy is more likely to be in the vicinity of a Sc atom when it is bound to a Si atom. Different Sc-Si-vacancy configurations, based on sub-lattice allocations of the vacancy, Sc and Si atoms, yield a binding energy in the range -0.17 to 0.08 eV vacancy⁻¹. These values are more positive than the Sc-vacancy binding energy of -0.25 eV vacancy⁻¹. Furthermore, the calculated value of the Sc migration energy in Al is decreased from 0.74 eV atom⁻¹ in the absence of Si to 0.45 eV atom⁻¹ for a configuration that results in Si-Sc binding following a Sc-vacancy interchange [44]. The calculations strengthen the hypothesis that the Sc diffusion kinetics is accelerated by additions of Si. Whether Si has the same effect on Er is unknown and should be studied in Al-Er-Si alloys.

4.4.2. Enhancement of precipitation strengthening

During isothermal aging at 400 °C (Fig. 6a), the improved alloy achieves a microhardness of 504 MPa after 0.5 h, and a peak microhardness of 533 MPa after 60 h of aging, while Si-free Al-0.05Sc-0.01Er-0.06Zr alloy [41] achieves 422 MPa after 0.5 h and a peak microhardness of 463 MPa after 380 h of aging. Given that the alloys have the same supersaturations as Sc, Zr and Er, this implies that 0.05 at.% Si is responsible for this effect, with Si enhancing

the Al₃(Sc,Zr,Er) precipitation kinetics, thereby increasing the strengthening of the alloy. After 0.5 h of aging at 400 °C, APT demonstrates that N_v in the improved alloy is $1.11 \pm 0.37 \times 10^{22} \text{ m}^{-3}$, $\phi = 0.235\%$, with $\langle R \rangle = 4.1 \pm 0.8 \text{ nm}$. Since the APT data for Al-0.05Sc-0.01Er-0.06Zr alloy are unavailable and the microhardness and electrical conductivity evolution of Al-0.05Sc-0.01Er-0.06Zr and Al-0.04Sc-0.02Er-0.06Zr alloys during isothermal aging at 400 °C are similar, the current data are compared with those of Al-0.04Sc-0.02Er-0.06Zr alloy. After 0.5 h of aging at 400 °C, APT demonstrates that N_v is $0.54 \pm 0.17 \times 10^{22} \text{ m}^{-3}$, with $\phi = 0.144\%$, and $\langle R \rangle = 3.7 \pm 0.3 \text{ nm}$. This comparison implies that Si increases both N_v and ϕ , while maintaining similar $\langle R \rangle$ values, which reduces the mean edge-to-edge inter-precipitate distance, thereby increasing the precipitate strengthening contribution, dominated by Orowan dislocation looping, in the improved alloy. With an attractive binding energy between Si and a vacancy, Si-vacancy clusters tend to act as heterogeneous nucleation sites [44]. A similar effect is observed in Al-Mg-Sc alloys, where Mg stimulates heterogeneous nucleation of Al₃Sc precipitates [52–54].

4.4.3. Reduction in coarsening resistance

Silicon additions to Al-Sc-Er-Zr alloys lead to a reduction in precipitate coarsening resistance [55]. This is confirmed by the microhardness evolution during isothermal aging at 400 °C (Fig. 6a), which exhibits an earlier decrease in the improved alloy after ~60 h compared with ~300 h for the Si-free alloys. APT results demonstrate that the precipitates coarsen from $\langle R \rangle = 4.1$ to 6.3 nm from 0.5 h to 66 days of aging in the improved alloy, while maintaining $\langle R \rangle = 3.7 \text{ nm}$ after the same aging period in the Al-0.04Sc-0.02Er-0.06Zr alloy [41]. In previous research, the present authors explained the excellent coarsening resistance of the latter alloy by the formation of a Zr-enriched shell encapsulating the precipitates, which acts as a diffusion barrier for Sc and Er in the precipitate core [31,41]. The reduced coarsening resistance due to Si additions can be explained by two possible mechanisms. First, formation of Si-Sc and Si-Er dimers (Section 4.4.1) increases the Sc and Er diffusivities in the Zr-enriched shell and/or in the α -Al matrix, thereby reducing the precipitate coarsening resistance. Secondly, Si also accelerates the Zr diffusion kinetics by the same mechanism as demonstrated for Sc in the α -Al matrix. If the Zr diffusivity is sufficiently large in the α -Al matrix at 400 °C, the Zr-enriched shell will no longer act as a diffusion barrier, owing to the coarsening of the Zr shell. The enhancement of the Zr diffusion kinetics caused by Si in Al-Zr alloys was reported earlier [56–58]. The two possible mechanisms responsible for reduction in precipitate coarsening resistance proposed herein could be validated by first-principles calculations.

4.4.4. Change in precipitate concentration profiles

Silicon additions also have a strong effect on the concentration profiles within precipitates (Figs. 5 and 8). In the

Si-free Al–0.04Sc–0.02Er–0.06Zr alloy, the precipitates consist of three distinct components (an Er-enriched core, a Sc-enriched inner shell and a Zr-enriched outer shell) as a result of the sequential precipitation following the values of the intrinsic diffusivities, $D_{\text{Er}} < D_{\text{Sc}} < D_{\text{Zr}}$ [41]. Solutes in L_{12} -ordered precipitates diffuse slowly owing to correlation effects, maintaining non-flat concentration profiles within the precipitates during aging [41]. In the improved alloy, the ordered precipitates consist of a homogenized mixture of Er, Sc and Si atoms in the core and a Zr-enriched shell (Figs. 5 and 8). The Er, Sc and Si mixture within the precipitate core is explainable by two possible mechanisms. First, Er diffuses faster than Sc in the α -Al matrix, resulting in the formation of an Er-enriched core and a Sc-enriched shell in Al–Sc–Er precipitates [11,13] and Al–Sc–Er–Zr [41] alloys. By forming Si–Er and Si–Sc dimers, addition of Si may increase the Sc diffusivity more than the Er diffusivity, which may result in equal diffusivity values, resulting in co-precipitation of Sc and Er, together with Si, during aging. Secondly, the Si addition possibly accelerates the Sc and Er diffusion kinetics within the L_{12} -ordered precipitates, thereby removing the concentration gradients within them caused by sequential precipitation. The possible mechanisms responsible for the changes in concentration profiles within the ordered precipitates may be validated using first-principles calculations. The change in an ordered precipitate's internal chemical structure may modify the elastic interaction between precipitates and dislocations, thus affecting the high-temperature creep strength [59]. This hypothesis is currently being studied [55].

5. Summary and conclusions

The properties of an improved cast aluminum alloy, Al–0.055Sc–0.005Er–0.02Zr–0.05Si at.%, were investigated by microhardness and electrical conductivity measurements, SEM and APT. The following conclusions are deduced from the experimental results:

1. Homogenization for at least 0.5 h at 640 °C is needed to eliminate Al_3Er primary precipitates, thus maximizing the Er supersaturation in the α -Al(fcc) matrix during aging and minimizing grain refinement, which is deleterious for high-temperature creep strength.
2. A Zr concentration as small as 0.02 at.% is sufficient to maintain the microhardness above ~ 430 MPa during isothermal aging at 400 °C for up to 66 days, by enhancing the precipitates' coarsening resistance, owing to the small diffusivity of Zr in the α -Al matrix.
3. After 0.5 h of aging at 400 °C, the improved alloy has $N_v = 1.11 \pm 0.37 \times 10^{22} \text{ m}^{-3}$, $\langle R \rangle = 4.1 \pm 0.8 \text{ nm}$, and $\phi = 0.235$, displaying a homogenized mixture of Sc, Er and Si within the ordered- L_{12} precipitates, surrounded by a shell slightly enriched in Zr in the precipitates. After 66 days of aging at 400 °C, it has $N_v = 0.20 \pm 0.10 \times 10^{22} \text{ m}^{-3}$, $\langle R \rangle = 6.3 \pm 0.3 \text{ nm}$,

and $\phi = 0.210$, with the precipitates consisting of an inner core, enriched in Sc, Er and Si, and an outer shell, enriched in Zr and smaller Er and Si concentrations.

4. Isothermal aging at 300 °C provides the largest peak microhardness, 606 ± 22 MPa after 1008 h of aging. Aging at higher temperatures results in smaller peak microhardness values. A two-step aging heat treatment, 1 h at 300 °C, to obtain a high number density of nuclei, and for 2 h at 375 °C, to increase the volume fraction of precipitates, appears to be optimal for achieving an excellent strength, ~ 570 MPa, in a reasonable aging time.
5. Addition of 0.05 at.% Si has three distinct advantages:
 - (a) It decreases the alloy's cost because Si is a common impurity in the commercial purity Al used.
 - (b) It enhances the strength by increasing the precipitate number density. Previous work [44] using first-principles calculation demonstrates an attractive binding energy between Si and a vacancy, Si–vacancy clusters might act as heterogeneous nucleation sites. Thus, addition of Si most likely causes heterogeneous nucleation of $\text{Al}_3(\text{Sc,Zr,Er})$ precipitates.
 - (c) It decreases the peak aging time by the accelerating precipitation kinetics of Sc and Er. This conclusion is based on results from previous work [44] using first-principles calculation, demonstrating that a vacancy is more likely to be in the vicinity of a Sc atom when it is bound to a Si atom. Moreover, the calculation shows that the Sc migration energy in Al is decreased when it binds to a Si atom. A similar effect is anticipated to occur for Er atoms.
6. Addition of Si, however, reduces the coarsening resistance of precipitates during aging at 400 °C. The Si-containing alloy exhibits an earlier decrease in microhardness compared with the Si-free alloys. Precipitates coarsen from $\langle R \rangle = 4.1$ to 6.3 nm from 0.5 h to 66 days of aging in the Si-containing alloy, while maintaining $\langle R \rangle = 3.7$ nm after the same aging period in the Si-free alloy. Two mechanisms are possible:
 - (a) Silicon accelerates diffusion of Sc and Er in the Zr-enriched outer shell, since a similar effect occurs in the α -Al(fcc) matrix.
 - (b) Silicon accelerates Zr diffusion kinetics within the α -Al(fcc) matrix by the same mechanism by which the Sc diffusivity is increased.
7. Addition of Si modifies the concentration profiles within precipitates, enhancing the chemical homogeneity of Sc and Er in the core, rather than forming the Er-enriched core/Sc-enriched shell observed in previous work [41]. There are two possible mechanisms:
 - (a) Silicon possibly promotes co-precipitation of Sc and Er to form $\text{Al}_3(\text{Sc,Er})$ in the α -Al(fcc) matrix.

- (b) Silicon accelerates the Sc and Er diffusion kinetics in the L1₂-ordered precipitate, driving the initial structure of Er-enriched core/Sc-enriched shell to the final structure of a homogeneous distribution of Sc and Er, a more thermodynamically favored state.

Acknowledgments

This research was sponsored by the Ford–Boeing–Northwestern University Alliance (81132882). APT was performed at the Northwestern University Center for Atom-Probe Tomography (NUCAPT). The LEAP tomography system was purchased and upgraded with funding from NSF-MRI (DMR-0420532) and ONR-DURIP (N00014-0400798, N00014-0610539 and N00014-0910781) grants. The authors also gratefully acknowledge the Initiative for Sustainability and Energy at Northwestern (ISEN) for grants to upgrade the capabilities of NUCAPT. They thank Drs. J. Boileau and B. Ghaffari (Ford), and Dr. R. Glamm (Boeing) for numerous useful discussions, Dr. D. Isheim (NU) for his assistance with atom-probe tomography, Mr. P. Bocchini (NU) for his assistance with casting, heat treatment, and many useful discussions, and Dr. I. Blum (NU) for his assistance with IVAS software.

Appendix A

Precipitate strengthening results from order strengthening, coherence strengthening, modulus mismatch strengthening or Orowan dislocation looping. Relationships for the yield strength increments $\Delta\sigma$ from each of these contributions of Al₃Sc(L1₂) precipitates in the α -Al(fcc) matrix [3,41] are now discussed. The order strengthening increment $\Delta\sigma_{\text{ord}}$ is given by

$$\Delta\sigma_{\text{ord}} = 0.81M \frac{\gamma_{\text{APB}}}{2b} \left(\frac{3\pi\phi}{8} \right)^{1/2} \quad (\text{A1})$$

where $M = 3.06$ is the mean matrix orientation factor for Al [60], $b = 0.286$ nm is the magnitude of the matrix Burgers vector [27], ϕ is the volume fraction of precipitates, and $\gamma_{\text{APB}} = 0.5$ J m⁻² is an average value of the Al₃Sc anti-phase boundary energy for the (111) plane [61–63].

The coherence strengthening increment $\Delta\sigma_{\text{coh}}$ is given by

$$\Delta\sigma_{\text{coh}} = M\alpha_{\varepsilon}(G\theta)^{3/2} \left(\frac{\langle R \rangle \phi}{0.5Gb} \right)^{1/2} \quad (\text{A2})$$

where $\alpha_{\varepsilon} = 2.6$ is a constant [64], $G = 25.4$ GPa is the shear modulus of Al [65], $\langle R \rangle$ is the average precipitate radius, and θ is the constrained lattice parameter mismatch at room temperature, calculated using Vegard's law [3,51], based on precipitate composition, as revealed by APT (Table 3).

The modulus mismatch strengthening increment $\Delta\sigma_{\text{mod}}$ is given by

$$\Delta\sigma_{\text{mod}} = 0.0055M(\Delta G)^{3/2} \left(\frac{2\phi}{Gb^2} \right)^{1/2} b \left(\frac{\langle R \rangle}{b} \right)^{(3m/2-1)} \quad (\text{A3})$$

where $\Delta G = 42.5$ GPa is the shear modulus mismatch between the matrix and the precipitates [66], and m is a constant taken as 0.85 [64].

The strengthening increment due to Orowan dislocation looping, $\Delta\sigma_{\text{Or}}$, is given by

$$\Delta\sigma_{\text{Or}} = M \frac{0.4}{\pi} \frac{Gb}{\sqrt{1-\nu}} \frac{\ln \left(\frac{2(\sqrt{\frac{2}{3}}\langle R \rangle)}{b} \right)}{\lambda} \quad (\text{A4})$$

where $\nu = 0.34$ is Poisson's ratio for Al [60]. The edge-to-edge inter-precipitate distance λ is taken to be the square-lattice spacing in parallel planes, which is given by [67]

$$\lambda = \left[\left(\frac{3\pi}{4\phi} \right)^{1/2} - 1.64 \right] \langle R \rangle \quad (\text{A5})$$

References

- [1] Toropova LS, Eskin DG, Kharakterova ML, Dobatkina TV. Advanced aluminum alloys containing scandium. New York: Gordon & Breach; 1998.
- [2] Marquis EA, Seidman DN. Acta Mater 2001;49:1909.
- [3] Seidman DN, Marquis EA, Dunand DC. Acta Mater 2002;50:4021.
- [4] Royset J, Ryum N. Int Mater Rev 2005;50:19.
- [5] Drits ME, Ber LB, Bykov YG, Toropova LS, Anastas'eva GK. Phys Met Phys Metall 1984;57:1172.
- [6] Drits ME, Dutkiewicz J, Toropova LS, Salawa. J Cryst Res Technol 1984;19:1325.
- [7] Vlach M, Stulikova I, Smola B, Zaludova N, Cerna J. J Alloys Compd 2010;492:143.
- [8] Jones MJ, Humphreys FJ. Acta Mater 2003;51:2149.
- [9] Royset J, Ryum N. Mater Sci Eng A 2005;396:409.
- [10] Watanabe C, Kondo T, Monzen R. Metall Mater Trans A 2004;35A:3003.
- [11] Karnesky RA, van Dalen ME, Dunand DC, Seidman DN. Scr Mater 2006;55:437.
- [12] van Dalen ME, Dunand DC, Seidman DN. J Mater Sci 2006;41:7814.
- [13] Karnesky RA, Dunand DC, Seidman DN. Acta Mater 2009;57:4022.
- [14] van Dalen ME, Karnesky RA, Cabotaje JR, Dunand DC, Seidman DN. Acta Mater 2009;57:4081.
- [15] Krug ME, Werber A, Dunand DC, Seidman DN. Acta Mater 2010;58:134.
- [16] Krug ME, Dunand DC, Seidman DN. Acta Mater 2011;59:1700.
- [17] Monachon C, Krug ME, Seidman DN, Dunand DC. Acta Mater 2011;59:3398.
- [18] Mao Z, Seidman DN, Woverton C. Acta Mater 2011;59:3659.
- [19] van Dalen ME, Dunand DC, Seidman DN. Acta Mater 2011;59:5224.
- [20] van Dalen ME, Gyger T, Dunand DC, Seidman DN. Acta Mater 2011;59:7615.
- [21] Krug ME, Seidman DN, Dunand DC. Mater Sci Eng A 2012;550:300.
- [22] Wen SP, Gao KY, Li Y, Huang H, Nie ZR. Scr Mater 2011;65:592.
- [23] Li H, Bin J, Liu J, Gao Z, Lu X. Scr Mater 2012;67:73.
- [24] Harada Y, Dunand DC. Mater Sci Eng A 2002;329–331:686.
- [25] Harada Y, Dunand DC. Scr Mater 2003;48:219.
- [26] Fuller CB, Seidman DN, Dunand DC. Acta Mater 2003;51:4803.
- [27] van Dalen ME, Dunand DC, Seidman DN. Acta Mater 2005;53:4225.
- [28] Fuller CB, Murray JL, Seidman DN. Acta Mater 2005;53:5401.
- [29] Fuller CB, Seidman DN. Acta Mater 2005;53:5415.
- [30] van Dalen ME, Seidman DN, Dunand DC. Acta Mater 2008;56:4369.

- [31] Knipling KE, Karnesky RA, Lee CP, Dunand DC, Seidman DN. *Acta Mater* 2010;58:5184.
- [32] Knipling KE, Seidman DN, Dunand DC. *Acta Mater* 2011;59:943.
- [33] Lefebvre W, Danoix F, Hallem H, Forbord B, Bostel A, Marthinsen K. *J Alloys Compd* 2009;470:107.
- [34] Belov NA, Alabin AN, Eskin DG, Istomin-Kastrovskii VV. *J Mater Sci* 2006;41:5890.
- [35] Forbord B, Lefebvre W, Danoix F, Hallem H, Marthinsen K. *Scr Mater* 2004;51:333.
- [36] Tolley A, Radmilovic V, Dahmen U. *Scr Mater* 2005;52:621.
- [37] Harada Y, Dunand DC. *Intermetallics* 2009;17:17.
- [38] Fuller CB, Seidman DN, Dunand DC. *Scr Mater* 1999;40:691.
- [39] Karnesky RA, Seidman DN, Dunand DC. *Mater Sci Forum* 2006;519–521:1035.
- [40] Krug ME. Microstructural evolution and mechanical properties in Al–Sc alloys with Li and rare Earth additions. Ph.D. dissertation. Northwestern University; 2011.
- [41] Booth-Morrison C, Dunand DC, Seidman DN. *Acta Mater* 2011;59:7029.
- [42] Hallem H, Lefebvre W, Forbord B, Danoix F, Marthinsen K. *Mater Sci Eng A* 2006;421:154.
- [43] Booth-Morrison C, Seidman DN, Dunand DC. *Acta Mater* 2012;60:3643.
- [44] Booth-Morrison C, Mao Z, Diaz M, Dunand DC, Wolverson C, Seidman DN. *Acta Mater* 2012;60:4740.
- [45] Davis JR. Aluminum and aluminum alloys. Metals Park, OH: ASM International; 1993.
- [46] Seidman DN. *Annu Rev Mater Res* 2007;37:127.
- [47] Kelly TF, Miller MK. *Rev Sci Instrum* 2007;78:031101.
- [48] Parratt LG. Probability and experimental errors in science. New York: John Wiley; 1966.
- [49] Hellman OC, Vandenbroucke JA, Rusing J, Isheim D, Seidman DN. *Microsc Microanal* 2000;6:437.
- [50] Marumo T, Fujikawa S, Hirono K. *J Jpn Inst Met* 1973;23:17.
- [51] Knipling KE, Dunand DC, Seidman DN. *Z Metallkd* 2006;97:246.
- [52] Marquis EA, Seidman DN. *Surf Interface Anal* 2004;36:559.
- [53] Marquis EA, Seidman DN, Asta M, Woodward C. *Acta Mater* 2006;54:119.
- [54] Vo NQ, Dunand DC, Seidman DN. *Acta Mater* 2012;60:7078.
- [55] Vo NQ, Dunand DC, Seidman DN [in preparation].
- [56] Ohashi T, Ichikawa R. *J Jpn Inst Met* 1970;34:604.
- [57] Sato T, Kamio A, Lorimer GW. *Mater Sci Forum* 1996;217–222: 895.
- [58] Hori S, Kondo T, Ikeno S. *J Jpn Inst Light Met* 1978;28:79.
- [59] Krug ME, Dunand DC. *Acta Mater* 2011;59:5125.
- [60] Meyers M, Chawla K. Mechanical metallurgy: principles and applications. Englewood Cliffs, NJ: Prentice Hall; 1984.
- [61] Fu C. *J Mater Res* 1990;5:971.
- [62] George E, Pope D, Fu C, Schneibel J. *ISIJ Int* 1991;31:1063.
- [63] Fukunaga K, Shouji T, Miura Y. *Mater Sci Eng A* 1997;239:202.
- [64] Ardell AJ. *Metall Mater Trans A* 1985;16A:2131.
- [65] Frost H, Ashby M. Deformation mechanism maps. Oxford: Pergamon Press; 1982.
- [66] Hyland R, Stiffler R. *Scr Metall Mater* 1991;25:473.
- [67] Nembach E. Particle strengthening of metals and alloys. New York, NY: John Wiley; 1997.